

Three-dimensional Radial Visualization of High-dimensional Datasets with Mixed Features

Yifan Zhu, Fan Dai and Ranjan Maitra

Abstract—We develop methodology for 3D radial visualization (RadViz) of high-dimensional datasets. Our display engine is called RadViz3D and extends the classical 2D RadViz that visualizes multivariate data in the 2D plane by mapping every record to a point inside the unit circle. We show that distributing anchor points at least approximately uniformly on the 3D unit sphere provides a better visualization with minimal artificial visual correlation for data with uncorrelated variables. Our RadViz3D methodology therefore places equi-spaced anchor points, one for every feature, exactly for the five Platonic solids, and approximately via a Fibonacci grid for the other cases. Our Max-Ratio Projection (MRP) method then utilizes the group information in high dimensions to provide distinctive lower-dimensional projections that are then displayed using RadViz3D. Our methodology is extended to datasets with discrete and continuous features where a Gaussianized distributional transform is used in conjunction with copula models before applying MRP and visualizing the result using RadViz3D. A R package `radviz3d` implementing our complete methodology is available.

Index Terms—copula models, generalized distributional transform, Indic scripts, principal components, RNA sequences, SVD



1 INTRODUCTION

MODERN applications often yield datasets of many dimensions and complexity. Visualizing such data is important to gain insight into their properties and the similarity or distinctiveness of different groups [1]. However, effective visualization can be challenging because the observations need to be mapped to a lower-dimensional space, with the reduced display conveying information on the characteristics as faithfully as possible. Such displays become even more difficult with mixed-features data, that is, when some of the attributes in the dataset are discrete.

Continuous multivariate data are displayed in many ways [2] (e.g. starplots [3], Chernoff faces [4], parallel coordinate plots [5], [6], surveyplots [7], Andrews' curves [8], [9], biplots [10], star coordinate plots [11], Uniform Manifold Approximation and Projections (UMAP) [12]), but our first focus in this paper is to improve radial visualization or RadViz [13], [14], [15], [16] that projects data onto a circle using Hooke's law. Here, p -dimensional observations are projected onto the 2D plane using p anchor points equally arranged to be on the perimeter of a circle. This representation places each observation at the center of the circle that is then pulled by springs in the directions of the p anchor points while being balanced by forces relative to the coordinate values. Observations with similar relative values across all attributes are then placed close to the center while

the others are placed closer to anchor points corresponding to the coordinates with higher relative values. However, there is loss of information [17] in RadViz which maps a p -dimensional point to 2D. This loss worsens with increasing p , but may potentially be alleviated by extending it to 3D. The Viz3D approach [17] extends 2D RadViz (henceforth, RadViz2D) by simply adding to the 2D projection a third projection direction that is constant for all features. Viz3D's improvement over RadViz2D is limited, so we investigate the possibility of developing a truly 3D extension of RadViz. We call our method RadViz3D and develop it in Section 2.1.

Our second major objective is to improve visualization of high-dimensional datasets with mixed features. Section 2.2 first develops a Max-Ratio Projection (MRP) method that linearly projects a labeled continuous-features dataset into a lower-dimensional space to allow for its effective visualization via RadViz3D while preserving its group-specific distinctiveness and variability. Our methodology is then extended to provide novel displays of datasets that also have discrete features. Specifically, we use the Gaussianized Distributional Transform (GDT) with copula models to render mixed-features datasets to the continuous space, after which MRP and RadViz3D can be used.

Beyond Section 2, the paper is organized as follows. Section 3 illustrates the ability of our methodology to faithfully display labeled data of different separations. Section 4 illustrates our methodology on several high-dimensional datasets with mixed features. The main paper concludes with some discussion in Section 5. We also have supplementary materials that discuss available methods for displaying high-dimensional datasets, and an online resource at <https://fanne-stat.github.io/RadViz3DExperiments/index.html> that allows for the reader to visualize displays in 3D. Items in the online resource are referenced in this paper with the prefix "S".

Y. Zhu and R. Maitra are with the Department of Statistics at Iowa State University, Ames, Iowa 50011, USA. e-mail: {yifanzhu,maitra}@iastate.edu. F. Dai is with the Department of Mathematical Sciences at the Michigan Technological University, Houghton, Michigan 49931, USA. e-mail: fand@mtu.edu.

©201x IEEE. Personal use of this material is permitted. However, permission to use this material for any other purposes must be obtained from the IEEE by sending a request to pubs-permissions@ieee.org.

Manuscript received xxxx xx,201x; revised xxxxxxxx xx, 201x. First published xxxxxxxx x, xxxx, current version published yyyyyyyy y, yyyy

Digital Object Identifier

2 METHODOLOGY

2.1 Radial Visualization

2.1.1 Background and Preliminary Development

We first define generalized radial visualization (GRadViz) as a natural extension of the classic RadViz2D that maps $\mathbf{X} = (X_1, X_2, \dots, X_p)' \in \mathcal{R}^p$ to a 2D point using

$$\Psi^\bullet(\mathbf{X}; \mathbf{U}) = \frac{\mathbf{U}\mathbf{X}}{\mathbf{1}_p'\mathbf{X}}, \quad (1)$$

where $\mathbf{1}_p = (1, 1, \dots, 1)'$, and $\mathbf{U} = [\mathbf{u}_1, \mathbf{u}_2, \dots, \mathbf{u}_p]$ is a projection matrix, where the j th column \mathbf{u}_j is the j th anchor point on $\mathbb{S}^1 = \{\mathbf{x} \in \mathcal{R}^2 : \|\mathbf{x}\| = 1\}$ for $j = 1, 2, \dots, p$. These p anchor points are equi-spaced on \mathbb{S}^1 . GRadViz uses a transformation $\Psi(\cdot; \cdot)$ similar to $\Psi^\bullet(\cdot; \cdot)$ in (1) but the anchor points in \mathbf{U} are allowed to lie on a hypersphere \mathbb{S}^q , $q > 1$ and are not necessarily equi-spaced on \mathbb{S}^q .

As in RadViz2D, our generalization $\Psi(\cdot; \cdot)$ also has a physical interpretation. Suppose that we have p springs connected to the anchor points $\mathbf{u}_1, \mathbf{u}_2, \dots, \mathbf{u}_p \in \mathbb{S}^q$ and that these p springs have spring constants X_1, X_2, \dots, X_p . Let $\mathbf{Y} \in \mathcal{R}^{q+1}$ be the equilibrium point of the system. Then

$$\sum_{j=1}^p X_j(\mathbf{Y} - \mathbf{u}_j) = 0,$$

with our generalization $\mathbf{Y} = \Psi(\mathbf{X}; \mathbf{U})$ as its solution.

GRadViz is actually a special case of normalized radial visualization (NRV) [18] that allows the anchor points to lie outside the hypersphere and is line-, point-ordering- and convexity-invariant. These desirable properties for visualization are also inherited by $\Psi(\cdot; \cdot)$. Also, GRadViz is scale-invariant, i.e., $\Psi(k\mathbf{X}; \mathbf{U}) = \Psi(\mathbf{X}; \mathbf{U})$ for any $k \neq 0$. That is, a line passing through the origin is projected to a single point in the radial visualization. So, we need to avoid a situation where all the observations are approximately on a line passing through the origin. The minmax transformation on the j th feature of the i th record

$$m_j(X_{ij}) = \frac{X_{ij} - \min_{1 \leq i \leq n} X_{ij}}{\max_{1 \leq i \leq n} X_{ij} - \min_{1 \leq i \leq n} X_{ij}} \quad (2)$$

guards against this eventuality. It also places every record in $[0, 1]^p$, ensuring that the data after also applying $\Psi(\cdot; \cdot)$ are all inside the unit ball $\mathbb{B}^{q+1} = \{\mathbf{x} \in \mathcal{R}^{q+1} : \|\mathbf{x}\| \leq 1\}$.

The placement of the anchor points is another issue in GRadViz, with different points yielding very different visualizations. Now suppose that \mathbf{X} has p uncorrelated coordinates. For any $\mathbf{X}_1, \mathbf{X}_2 \in \mathcal{R}^p$, let $\mathbf{Y}_i = \Psi(\mathbf{X}_i; \mathbf{U})$, $i = 1, 2$ be the GRadViz-transformed data. The Euclidean distance between \mathbf{Y}_1 and \mathbf{Y}_2 is

$$\|\mathbf{Y}_1 - \mathbf{Y}_2\|^2 = \left(\frac{\mathbf{X}_1}{\mathbf{1}_p'\mathbf{X}_1} - \frac{\mathbf{X}_2}{\mathbf{1}_p'\mathbf{X}_2} \right)' \mathbf{U}'\mathbf{U} \left(\frac{\mathbf{X}_1}{\mathbf{1}_p'\mathbf{X}_1} - \frac{\mathbf{X}_2}{\mathbf{1}_p'\mathbf{X}_2} \right),$$

a quadratic form with positive definite matrix $\mathbf{U}'\mathbf{U}$ that has the i th diagonal element $\mathbf{u}_i'\mathbf{u}_i = 1$ and (i, j) th entry $\mathbf{u}_i'\mathbf{u}_j = \cos\langle \mathbf{u}_i, \mathbf{u}_j \rangle$. For $\mathbf{X}_l = a_l \mathbf{e}_l$, for $l = i, j$, with \mathbf{e}_i having 1 in the i th position and 0 elsewhere,

$$\|\mathbf{Y}_i - \mathbf{Y}_j\|^2 = 2 - 2\cos\langle \mathbf{u}_i, \mathbf{u}_j \rangle. \quad (3)$$

The i th and j th coordinates of \mathbf{X}_i and \mathbf{X}_j in this example are as dissimilar as possible from each other, having perfect

negative correlation, and should be placed as far apart as possible (in opposite directions) in the radial visualization. However (3) shows that the distance between \mathbf{Y}_i and \mathbf{Y}_j approaches 0 as the angle between \mathbf{u}_i and \mathbf{u}_j approaches 0. Therefore, the radial visualization can create artificial visual correlation between the i th and j th coordinates if the angle between \mathbf{u}_i and \mathbf{u}_j is less than $\pi/2$. (As a corollary, strongly positively correlated coordinates should be placed as close together as possible.) To reduce such effects, we need to distribute the anchor points as far away from each other as possible. This leads to evenly-distributed anchor points on \mathbb{S}^q for our GRadViz formulation. RadViz3D has an inherent advantage over RadViz2D because it can more readily facilitate larger angles between anchor points. (indeed, higher-dimensional displays beyond 3D would be even more beneficial were it possible to have such displays.) This is because the smallest angle between any two of p (fixed) evenly-distributed anchor points in RadViz3D is always larger than that in RadViz2D. For example, with $p = 4$, we can place anchor points so that the angle between any two of them is the same, but this is not possible in 2D. At the same time, RadViz2D can not place multiple positively correlated coordinates next to each other at the same time, as desirable for accurate visualization [19]. The placement of anchor points therefore plays an important role in RadViz2D [20], [21], but is less pronounced with RadViz3D.

Our discussion on GRadViz has provided the rationale behind RadViz3D with equi-spaced anchor points. We are now ready to formalize the construction of RadViz3D.

2.1.2 RadViz3D

We develop RadViz3D for observations with p continuous-valued coordinates. Following the discussion in Section 2.1.1, let $\Psi : \mathcal{R}^p \mapsto \mathbb{B}^3 = \{\mathbf{x} \in \mathcal{R}^3 : \|\mathbf{x}\| \leq 1\}$ map $\mathbf{X} \in \mathcal{R}^p$ to $\Psi(\mathbf{X}; \mathbf{U}) = \mathbf{U}\mathbf{X}/\mathbf{1}_p'\mathbf{X}$ with \mathbf{U} as before and with j th column (anchor point) \mathbf{u}_j , that we have contended, should be as evenly-spaced in \mathbb{S}^2 as possible. We find the set \wp of equi-spaced anchor points $\mathbf{u}_1, \mathbf{u}_2, \dots, \mathbf{u}_p$ from Result 1.

Result 1. Anchor Points Set. Denote the golden ratio by $\varphi = (1 + \sqrt{5})/2$. For $p = 4, 6, 8, 12, 20$, the elements in \wp have the coordinates listed in Table 1. For other integers $p \geq 5$, only an

TABLE 1: Anchor points set for $p \in \{4, 6, 8, 12, 20\}$. Here $\varphi = (1 + \sqrt{5})/2$.

p	Platonic Solid	\wp
4	Tetrahedron	$\{(1, 1, 1)/\sqrt{3}, (1, -1, -1)/\sqrt{3}, (-1, 1, -1)/\sqrt{3}, (-1, -1, 1)/\sqrt{3}\}$
6	Octahedron	$\{(\pm 1, 0, 0), (0, \pm 1, 0), (0, 0, \pm 1)\}$
8	Cube	$\{\pm 1, \pm 1, \pm 1\}$
12	Icosahedron	$\{(0, \pm 1, \pm \varphi), (\pm 1, \pm \varphi, 0), (\pm \varphi, 0, \pm 1)\}/\sqrt{1 + \varphi^2}$
20	Dodecahedron	$\{(\pm 1, \pm 1, \pm 1)/\sqrt{3}, (0, \pm \varphi^{-1}, \pm \varphi)/\sqrt{3}, (\pm \varphi^{-1}, \pm \varphi, 1)/\sqrt{3}, (\pm \varphi, 0, \pm \varphi^{-1})/\sqrt{3}\}$

approximate solution is possible: here the elements of \wp are $\mathbf{u}_j = (u_{j1}, u_{j2}, u_{j3})$, $j = 1, 2, \dots, p$ with $u_{j1} = \cos(2\pi j \varphi^{-1})(1 - u_{j3}^2)^{-\frac{1}{2}}$, $u_{j2} = \sin(2\pi j \varphi^{-1})(1 - u_{j3}^2)^{-\frac{1}{2}}$, $u_{j3} = (2j - 1)/p - 1$.

Proof. For $p = 4, 6, 8, 12, 20$, the coordinates are exactly equi-spaced with anchor points corresponding to the ver-

tices of the Platonic solids. For other values of $p \geq 5$, we derive an approximate solution by implementing a Fibonacci grid method [22] that produces the latitude ϕ_j and longitude θ_j of the j th anchor point on \mathbb{S}^3 as $\phi_j = \arcsin a_j, \theta_j = 2\pi j\varphi^{-1}$ with a_1, a_2, \dots, a_p an arithmetic progression chosen to have common difference $2/p$. We take $a_1 = 1/p - 1$, so $a_j = 2(j-1)/p + a_1 = (2j-1)/p - 1$. Then, the Cartesian coordinate of the j th anchor point $\mathbf{u}_j \in \wp$ follows by transforming between coordinate systems. \square

Remark 2. The geometric solutions of \wp for $p \in \{4, 6, 8, 12, 20\}$ are closely related to the Thomson problem in traditional molecular quantum chemistry [23]. Also, for $p \geq 5, p \notin \{4, 6, 8, 12, 20\}$, the approximate solution distributes anchor points along a generative spiral on \mathbb{S}^2 , with consecutive points as separated from each other as possible, satisfying the “well-separation” property [24].

Result 1 provides the wherewithal for RadViz3D for $p \geq 4$ by projecting each observation $\mathbf{X}_i \in \mathbb{R}^p, i = 1, 2, \dots, n$ to $\Psi(\mathbf{X}_i; \mathbf{U} = [\mathbf{u}_1, \dots, \mathbf{u}_p])$. RadViz3D displays of multidimensional data can then be obtained using 3D graphics to facilitate the discovery of patterns and structure.

2.2 Visualizing High-dimensional Datasets

With the machinery for RadViz3D in place, we now investigate methods for summarizing labeled high-dimensional data with mixed features. We first develop methods for high-dimensional continuous datasets and then extend to datasets that also have discrete features.

2.2.1 Datasets with Continuous Features

For even moderate dimensions ($p > 10$), displaying many anchor points is not helpful even after factoring in the benefits of going to 3D. Also our placement of equi-spaced anchor points is built upon not inducing spurious positive correlations in the display, and therefore using coordinates that do not, as far as possible, induce positive correlations in the display. So we project our high-dimensional datasets into a lower-dimensional space such that the projected coordinates are almost uncorrelated. A common approach to finding uncorrelated projections is Principal Components Analysis (PCA) that finds the mutually orthogonal projections summarizing a proportion of the total variance in the data. We propose using PCA for unlabeled data. For labeled data, approaches beyond PCA that exploit class labels [25] are desired. Our objective is to find an approach that preserves the distinctiveness of group labels when finding projections while also preserving, in the display, the inherent variability in the dataset. We develop Max-Ratio Projections (MRPs) of the data that maximizes separation between groups (in projected space) relative to its total variability. We discuss obtaining these projections next.

2.2.1.1 Directions that Maximize Between-Group Variance: Given a labeled dataset, we find a linear subspace such that the groups are well-separated when the data are projected along this subspace. Let $\mathbf{v}_1, \mathbf{v}_2, \dots, \mathbf{v}_k$ be k uncorrelated direction vectors spanning the linear subspace. In order to separate the groups, we want to project the data to each \mathbf{v}_j such that the ratio of the projected between-group sum of squares and the total corrected sum of squares is

maximized (equivalently, the ratio of the projected within-group sums of squares and the total corrected sum of squares is minimized).

Let $\Xi = \{\mathbf{X}_1, \mathbf{X}_2, \dots, \mathbf{X}_n\}$ be n p -dimensional observation vectors. Then the corrected total sum of squares and cross-products (SSCP) matrix is $\mathbf{T} = (n-1)\hat{\Sigma}$ where $\hat{\Sigma}$ is the sample dispersion matrix of Ξ . Let $\text{Var}(\mathbf{X}_i) = \Sigma$, then for any projection vector \mathbf{v}_j , we have $\text{Var}(\mathbf{v}_j' \mathbf{X}_i) = \mathbf{v}_j' \Sigma \mathbf{v}_j$. Further, for any two \mathbf{v}_j and \mathbf{v}_l , $\text{Cor}(\mathbf{v}_j' \mathbf{X}_i, \mathbf{v}_l' \mathbf{X}_i) \propto \mathbf{v}_j' \Sigma \mathbf{v}_l = 0$ since the direction vectors decorrelate the observed coordinates. (We may replace Σ with $\hat{\Sigma}$ in the expressions above.) Therefore, we obtain $\mathbf{v}_1, \mathbf{v}_2, \dots, \mathbf{v}_k$ in sequence to satisfy

$$\begin{aligned} \max_{\mathbf{v}_1} \frac{SS_{\text{group}}(\mathbf{v}_1)}{SS_{\text{total}}(\mathbf{v}_1)} \\ \max_{\mathbf{v}_j} \frac{SS_{\text{group}}(\mathbf{v}_j)}{SS_{\text{total}}(\mathbf{v}_j)} \quad \ni \quad \mathbf{v}_j' \mathbf{T} \mathbf{v}_i = 0, 1 \leq i < j \leq k \end{aligned} \quad (4)$$

where $SS_{\text{total}}(\mathbf{v}_l)$ is the corrected total sum of squares of the data projected along \mathbf{v}_l (so is a scalar quantity), and $SS_{\text{group}}(\mathbf{v}_l)$ is the corrected between-group sum of squares of the data projected along \mathbf{v}_l . Equivalently, if $SS_{\text{within}}(\mathbf{v}_l)$ is the corrected within-group sum of squares of data projected along \mathbf{v}_l , we know $SS_{\text{total}}(\mathbf{v}_l) = SS_{\text{group}}(\mathbf{v}_l) + SS_{\text{within}}(\mathbf{v}_l)$. Therefore the ratio can be written as

$$\frac{SS_{\text{within}}(\mathbf{v}_l)}{SS_{\text{total}}(\mathbf{v}_l)} = 1 - \frac{SS_{\text{group}}(\mathbf{v}_l)}{SS_{\text{total}}(\mathbf{v}_l)}.$$

Then the equivalent form of the optimization problem is

$$\begin{aligned} \min_{\mathbf{v}_1} \frac{SS_{\text{within}}(\mathbf{v}_1)}{SS_{\text{total}}(\mathbf{v}_1)} \\ \min_{\mathbf{v}_j} \frac{SS_{\text{within}}(\mathbf{v}_j)}{SS_{\text{total}}(\mathbf{v}_j)} \quad \ni \quad \mathbf{v}_j' \mathbf{T} \mathbf{v}_i = 0, 1 \leq i < j \leq k. \end{aligned} \quad (5)$$

Theorem 3. Max-Ratio Projections. Let $\mathbf{X}_1, \mathbf{X}_2, \dots, \mathbf{X}_n$ be p -dimensional observations from G groups. Let \mathbf{T} be the total corrected SSCP and \mathbf{B} be the corrected SSCP between groups. Let \mathbf{T} and \mathbf{B} both be positive definite. Then

$$\hat{\mathbf{v}}_j = \frac{\mathbf{T}^{-\frac{1}{2}} \hat{\mathbf{w}}_j}{\|\mathbf{T}^{-\frac{1}{2}} \hat{\mathbf{w}}_j\|}, \quad j = 1, 2, \dots, k \quad (6)$$

satisfies (4) where $\hat{\mathbf{w}}_j, j = 1, 2, \dots, k$ are the eigenvectors corresponding to the k largest eigenvalues of $\mathbf{T}^{-1/2} \mathbf{B} \mathbf{T}^{-1/2}$.

Proof. Let $\Gamma_g, g = 1, 2, \dots, G$ be the $n_g \times n$ matrix that selects observations from the matrix \mathbf{X} that has \mathbf{X}_i as its i th row. Here n_g is the number of observations from the g th group, for $g = 1, 2, \dots, G$. Then $\Gamma_g \mathbf{X}$ is the matrix with observations from the g th group in its rows and

$$\mathbf{B} = \mathbf{X}' \left(\sum_{g=1}^G \frac{1}{n_g} \Gamma_g' \mathbf{1}_{n_g} \mathbf{1}_{n_g}' \Gamma_g - \frac{1}{n} \mathbf{1}_n \mathbf{1}_n' \right) \mathbf{X} \quad (7)$$

and $\mathbf{T} = \mathbf{X}' (\mathbf{I}_n - \mathbf{1}_n \mathbf{1}_n' / n) \mathbf{X}$. Also, \mathbf{X} projected along any direction \mathbf{v} yields $SS_{\text{group}}(\mathbf{v}) = \mathbf{v}' \mathbf{B} \mathbf{v}$ and $SS_{\text{total}}(\mathbf{v}) = \mathbf{v}' \mathbf{T} \mathbf{v}$ so that finding (4) is equivalent to

$$\begin{aligned} \max_{\mathbf{v}_1} \frac{\mathbf{v}_1' \mathbf{B} \mathbf{v}_1}{\mathbf{v}_1' \mathbf{T} \mathbf{v}_1} \\ \max_{\mathbf{v}_j} \frac{\mathbf{v}_j' \mathbf{B} \mathbf{v}_j}{\mathbf{v}_j' \mathbf{T} \mathbf{v}_j} \quad \mathbf{v}_j' \mathbf{T} \mathbf{v}_i = 0, 1 \leq i < j \leq k. \end{aligned} \quad (8)$$

Let $\mathbf{w}_j = \mathbf{T}^{1/2} \mathbf{v}_j$, $j = 1, 2, \dots, k$. Then for each j ,

$$\frac{SS_{\text{group}}(\mathbf{v}_j)}{SS_{\text{total}}(\mathbf{v}_j)} = \frac{\mathbf{v}_j' \mathbf{B} \mathbf{v}_j}{\mathbf{v}_j' \mathbf{T} \mathbf{v}_j} = \frac{\mathbf{w}_j' \mathbf{T}^{-1/2} \mathbf{B} \mathbf{T}^{-1/2} \mathbf{w}_j}{\mathbf{w}_j' \mathbf{w}_j}$$

and $\mathbf{v}_j' \mathbf{T} \mathbf{v}_i = \mathbf{w}_j' \mathbf{w}_i$. Then, instead of (8), we can sequentially solve the following, with respect to $\mathbf{w}_1, \mathbf{w}_2, \dots, \mathbf{w}_k$:

$$\begin{aligned} \max_{\mathbf{w}_1} \frac{\mathbf{w}_1' \mathbf{T}^{-1/2} \mathbf{B} \mathbf{T}^{-1/2} \mathbf{w}_1}{\mathbf{w}_1' \mathbf{w}_1} \\ \max_{\mathbf{w}_j} \frac{\mathbf{w}_j' \mathbf{T}^{-1/2} \mathbf{B} \mathbf{T}^{-1/2} \mathbf{w}_j}{\mathbf{w}_j' \mathbf{w}_j} \quad \ni \quad \mathbf{w}_j' \mathbf{w}_i = 0, \quad 1 \leq i < j \leq k. \end{aligned} \quad (9)$$

$\mathbf{T}^{-1/2} \mathbf{B} \mathbf{T}^{-1/2}$ is nonnegative definite, with at most $G - 1$ positive eigenvalues, so $k \leq G - 1$ in (9). Its eigenvectors $\hat{\mathbf{w}}_1, \hat{\mathbf{w}}_2, \dots, \hat{\mathbf{w}}_k$ (corresponding to its k largest eigenvalues in decreasing order) solve (9). Let $\hat{\mathbf{v}}_j$ be the normalized version of $\mathbf{T}^{-1/2} \hat{\mathbf{w}}_j$. Then $\hat{\mathbf{v}}_j$ s satisfy (8). The theorem follows. \square

Theorem 3 provides the projections that maximize separation between the groups in a lower-dimensional space in a way that also decorrelates the coordinates. The number of projections is limited by $G - 1$. So, for $G \leq 3$, 1 to 2 projections and therefore 1D or 2D displays should be enough. (For $G = 3$, a RadViz2D figure should normally suffice, but, as we show later in our examples, choosing 4 projections yields a better display even though the additional $4 - G + 1$ projections yield no additional information on group separation. We use springs to provide a physical interpretation for why these additional $4 - G + 1$ coordinates are beneficial. The first $G - 1$ MRP coordinates pull the data with different forces along the corresponding anchor points in a way that permits maximum separation of the classes. The remaining $4 - G + 1$ anchor points correspond to the zero eigenvalues and do not contribute to the separation between groups, and so each group is pulled with equal force in the direction of these anchor points. These additional pulls separate the groups better in RadViz3D than in RadViz2D. (We choose 4 MRPs when $G \leq 4$ for RadViz3D because a 3D sphere is best separated using 4 equi-spaced anchor points because every axis is then equidistant to the other.)

The eigenvalue decomposition of $\mathbf{T}^{-1/2} \mathbf{B} \mathbf{T}^{-1/2}$ assumes a positive definite \mathbf{T} , for which a sufficient condition is that $n_g > p$ for all g . This assumption may not always hold so we now propose to reduce the dimensionality of the dataset for the cases where $p \geq \min_g n_g$ while also preserving as far as possible its group-specific features and variability.

2.2.1.2 Nearest Projection Matrix to Group-Specific Principal Components (PCs): Our approach builds on standard PCA whose goal, it may be recalled, is to project a dataset onto a lower-dimensional subspace in a way that captures most of its total variance. We use projections that summarize the variability within each group. So, we summarize each group by obtaining PCs separately and then finding the closest projection matrix to all the group-specific PCs. Specifically, we have the following

Result 4. Suppose that $\mathbf{V}_1, \mathbf{V}_2, \dots, \mathbf{V}_m$ are $p \times q$ matrices with $\mathbf{V}_j' \mathbf{V}_j = \mathbf{I}_q$, where \mathbf{I}_q is the $q \times q$ identity matrix. Let $\mathbf{V} = \sum_{j=1}^m \mathbf{V}_j$ with singular value decomposition (SVD)

$\mathbf{V} = \mathbf{P} \mathbf{\Lambda} \mathbf{Q}'$ where \mathbf{P} is a $p \times q$ matrix of orthogonal columns, \mathbf{Q} is a $q \times q$ orthogonal matrix and $\mathbf{\Lambda}$ is a $q \times q$ diagonal matrix with v non-zero entries where $v = \text{rank}(\mathbf{V})$. Then the $p \times q$ matrix $\mathbf{W} = \mathbf{P} \mathbf{Q}'$ satisfies

$$\mathbf{W} = \underset{\mathbf{W}}{\text{argmin}} \left\{ \sum_{j=1}^m \|\mathbf{W} - \mathbf{V}_j\|_F^2 : \mathbf{W}' \mathbf{W} = \mathbf{I}_q \right\}. \quad (10)$$

Proof. (Several proofs for Result 4 [26] exist but we provide a novel alternative proof to add to the literature.) Minimizing $\sum_{j=1}^m \|\mathbf{W} - \mathbf{V}_j\|_F^2$ is the same as maximizing $\sum_{j=1}^m \text{trace}(\mathbf{W}' \mathbf{V}_j)$ or, equivalently, $\text{trace}(\mathbf{W}' \mathbf{V})$. Let the full SVD of $\mathbf{V} = [\mathbf{P}_\bullet, \mathbf{P}_0][\mathbf{\Lambda}_\bullet, 0]\mathbf{Q}'$, where the i th diagonal element of $\mathbf{\Lambda}_\bullet$ is the nonnegative eigenvalue λ_i . Then $\text{trace}(\mathbf{W}' \mathbf{V}) = \text{trace}(\mathbf{Q}' \mathbf{W}' [\mathbf{P}_\bullet, \mathbf{P}_0][\mathbf{\Lambda}_\bullet, 0])$. Let $\mathbf{B} = \mathbf{Q}' \mathbf{W}' [\mathbf{P}_\bullet, \mathbf{P}_0]$ have b_{ij} as its (i, j) th entry. Then $\mathbf{B} \mathbf{B}' = \mathbf{I}_q$ and $|b_{ij}| \leq 1$ for all i, j . So, $\text{trace}(\mathbf{W}' \mathbf{V}) \leq |\text{trace}(\mathbf{W}' \mathbf{V})| = |\sum_{i=1}^v \lambda_i b_{ii}| \leq \sum \lambda_i |b_{ii}| \leq \sum \lambda_i = \text{trace}(\mathbf{\Lambda}_\bullet)$, with equality holding when $\mathbf{W} = \mathbf{P}_\bullet \mathbf{Q}'$. \square

Result 4 reduces dimensionality of a dataset for when the number of features is larger than the minimum number of records in any group. We take $m = \min\{p, n_1, n_2, \dots, n_g\}$. The k MRPs of our dataset are displayed using RadViz3D. The choice of k may be based on the clarity of the display, or by the cumulative proportion (we use 90%) of the eigenvalues of $\mathbf{T}^{-1/2} \mathbf{B} \mathbf{T}^{-1/2}$. Algorithm 1 summarizes how to obtain the MRPs of a labeled dataset Ξ with data matrix \mathbf{X} .

Algorithm 1 Max-Ratio Projection (MRP) Method

- 1: Remove the group mean for each observation in Ξ .
 - 2: Obtain the $p \times q$ eigenvector matrices $\mathbf{V}_1, \mathbf{V}_2, \dots, \mathbf{V}_G$ for each of the G groups where $q = \min\{p, n_1, n_2, \dots, n_g\}$.
 - 3: Use Result 4 to obtain the nearest orthogonal matrix \mathbf{W} to $\mathbf{V}_1, \mathbf{V}_2, \dots, \mathbf{V}_G$.
 - 4: Project the dataset to the new space of \mathbf{W} .
 - 5: Use Theorem 3 to find the projection matrix \mathbf{V} maximizing the between-group variance of the projected data.
 - 6: The matrix \mathbf{XV} provides the MRPs of the dataset.
-

Remark 5. We compare MRP with orthogonal linear discriminant analysis (OLDA) [27] and uncorrelated linear discriminant analysis (ULDA) [28]. OLDA also produces orthogonal discriminant vectors that project data onto a lower-dimensional subspace, however the projection vectors satisfy $\mathbf{v}_i' \mathbf{v}_j = 0$, $i \neq j$. This does not necessarily mean uncorrelated projections of the data since $\mathbf{v}_j' \Sigma \mathbf{v}_i$ is not necessarily zero. In our visualization, $\mathbf{v}_i' \Sigma \mathbf{v}_j = 0$, $i \neq j$ is desired and MRP satisfies this by producing uncorrelated projection directions. On the other hand, ULDA uses the same set of uncorrelated projection directions as MRP. However, MRP uses the normalized vectors (columns of projection matrix) with unit length, while the column vectors of the ULDA projection matrix are not normalized. Specifically, both ULDA and MRP have $\mathbf{v}_i' \Sigma \mathbf{v}_j = 0$, $i \neq j$, but in ULDA, $\mathbf{v}_i' \Sigma \mathbf{v}_i = 1$, while in MRP, $\mathbf{v}_i' \mathbf{v}_i = 1$. So the ULDA is actually MRP with a scaling step after the projection, such that each coordinate's variance is 1. In that sense, MRP can display a better visualization as the variance of for each projection direction is preserved.

2.2.2 Visualizing Discrete- and Mixed-Feature Datasets

Datasets with discrete features are complicated to visualize, but arise in genomics, survey and voting preferences

and other applications. We develop visualization methods by transforming these datasets using copulas specifically constructed to describe the correlation structure among the discrete variables in the joint distribution while maintaining the empirical marginal distribution. After transformation, we apply Section 2.2.1 for their visualization. We transform mixed-feature datasets using copulas, for which we introduce the generalized distributional transformation.

Definition 6 (Generalized Distributional Transform, [29], Chapter 1). Let Y be a real-valued random variable (RV) with cumulative distribution function (CDF) $F(\cdot)$ and let V be a RV independent of Y , such that $V \sim \text{Uniform}(0, 1)$. The generalized distributional transform of Y is $U = F(Y, V)$ where $F(y, \lambda) \doteq P(Y < y) + \lambda P(Y = y) = F(y-) + \lambda\{F(y) - F(y-)\}$ is the generalized CDF of Y , and $F(y-)$ is the left limit of $F(\cdot)$ at y .

Theorem 7 ([29], Chapter 1). Let $U = F(Y, V)$ be the distributional transform of Y as per Definition 6. Then

$$U \sim \text{Uniform}(0, 1) \text{ and } Y = F^{-1}(U) \text{ a.s.}$$

where $F^{-1}(t) = \inf\{y \in \mathcal{R} : F(y) \geq t\}$ is the generalized inverse, or the quantile transform, of $F(\cdot)$.

Suppose that $\mathbf{Y}_1, \mathbf{Y}_2, \dots, \mathbf{Y}_n$ is a sample of discrete-valued random vectors, each of which has the same distribution as $\mathbf{Y}_1 = (Y_{11}, Y_{12}, \dots, Y_{1p})$, where each margin Y_{1i} has CDF $F_i(\cdot)$ (a step function). Let $U_i = F(Y_{1i}, V_i)$. From Theorem 7, $U_i \sim \text{Uniform}(0, 1)$, so $(U_1, U_2, \dots, U_p) \sim C$ is a copula. Further, from the definition of a quantile transform and Theorem 7, the joint distribution for \mathbf{Y}_1 can be specified in terms of $F_i(\cdot)$ s and the constructed copula C as

$$\begin{aligned} F(y_1, y_2, \dots, y_p) &= \mathbb{P}(Y_{11} \leq y_1, Y_{12} \leq y_2, \dots, Y_{1p} \leq y_p) \\ &= \mathbb{P}[F_i^{-1}(U_i) \leq y_i \forall i = 1, 2, \dots, p] \\ &= \mathbb{P}[U_i \leq F_i(y_i) \forall i = 1, 2, \dots, p] \\ &= C[F_1(y_1), F_2(y_2), \dots, F_p(y_p)]. \end{aligned}$$

Now, we pick p continuous marginal distributions, each with CDF $\tilde{F}_i(\cdot)$, $i = 1, 2, \dots, p$. Then $(\tilde{F}_1^{-1}(U_1), \tilde{F}_2^{-1}(U_2), \dots, \tilde{F}_p^{-1}(U_p))$ has a continuous joint distribution with marginals $\tilde{F}_i(\cdot)$, $i = 1, 2, \dots, p$, and the copula associated with this joint distribution is also C .

We use the marginal empirical CDF (ECDF) $\hat{F}_i(\cdot)$ of the \mathbf{Y}_j s to estimate $F_i(\cdot)$ for $i = 1, 2, \dots, p$. We use $\mathcal{N}(0, 1)$ as the continuous marginals, i.e. $\tilde{F}_i(\cdot) = \Phi(\cdot)$, the $\mathcal{N}(0, 1)$ CDF. We define the Gaussianized distributional transform (GDT)

$$G(\mathbf{Y}_j, \mathbf{V}_j) \doteq [[\Phi^{-1}(\hat{F}_i(Y_{ji}, V_{ji}))]]_{i=1,2,\dots,p} \quad (11)$$

for $j = 1, 2, \dots, n$. Here $\mathbf{V}_j = (V_{j1}, V_{j2}, \dots, V_{jp})$, and V_{ji} s are independent identically distributed standard uniform realizations. Then $\mathbf{X}_i = G(\mathbf{Y}_i, \mathbf{V}_i)$, $i = 1, 2, \dots, n$ are realizations from a distribution on \mathcal{R}^p : we apply the methods of Section 2.2.1 on $\mathbf{X}_1, \mathbf{X}_2, \dots, \mathbf{X}_n$ before visualizing the resulting MRPs using RadViz3D.

Remark 8. We make a few comments on our use of the GDT:

- 1) For a continuous random variable, Theorem 7 reduces to the usual CDF so $G(\cdot, \cdot)$ can be applied also to datasets with mixed (continuous and discrete) features.
- 2) The GDT is a more stringent standardization than the usual affine transformation that only sets a dataset to

have zero mean and unit variance, because it transforms the marginal ECDFs to $\Phi(\cdot)$. So the GDT may, also be applied to datasets with skewed continuous features.

- 3) When datasets have discrete features with little class-discriminating ability, applying the GDT on such features will inflate the variance in the transformed space, resulting in a standard normal coordinate that is independent of the other features. When the number of such coordinates is substantial relative to group-discriminating features, these independent $\mathcal{N}(0, 1)$ -transformed coordinates will drive the MRP, resulting in poor separation. So we use an analysis of variance (ANOVA) test on each copula-transformed coordinate to ascertain if it contains significant group-discriminating information. Multiple significance issues are addressed by correcting for false discoveries [30]. Features so ascertained to not have significant discriminating information are dropped from the MRP and subsequent steps.

Algorithm 2 summarizes the use of GDT and MRP for mixed-features datasets.

Algorithm 2 RadViz3D for datasets with mixed features

- 1: Calculate the marginal ECDF $\hat{F}_1(\cdot), \hat{F}_2(\cdot), \dots, \hat{F}_p(\cdot)$ for each of the p coordinates of the dataset.
 - 2: Simulate $\mathbf{V}_i \stackrel{iid}{\sim} \text{Uniform}[0, 1]^p$.
 - 3: Construct the transform $G(\cdot, \cdot)$ with marginal ECDFs and simulated \mathbf{V}_i , $i = 1, 2, \dots, n$, as in Equation 11.
 - 4: Transform \mathbf{Y}_i in the discrete dataset to \mathbf{X}_i with $\mathbf{X}_i = G(\mathbf{Y}_i, \mathbf{V}_i)$, $i = 1, 2, \dots, n$.
 - 5: Apply MRP on \mathbf{X}_i , $i = 1, 2, \dots, n$ via Algorithm 1.
 - 6: Display MRP results by RadViz3D.
-

3 ILLUSTRATIVE PERFORMANCE EVALUATIONS

We illustrate RadViz3D on simulated 100D datasets of $n = 500$ observations from five groups with both discrete and continuous features and of known group separation and clustering complexity. The MIXSIM package [31] in R [32] allows for the simulation of (continuous) class data according to a pre-specified *generalized overlap* ($\tilde{\omega}$) [33], [34] that indexes clustering complexity, with very small values ($\tilde{\omega} = 0.001$) implying very good separation between groups and larger values ($\tilde{\omega} = 0.05$) indicating poorer separation and increased overlap. We discretize the first 50 coordinates in each group into 10 classes, based on the marginal deciles of the coordinate. We use the GDT and MRP on this mixed-features dataset and visualize using RadViz3D. Because of how our mixed-features datasets were generated, the MIXSIM-estimated pairwise overlaps between the 5 groups are essentially preserved (and displayed in the left columns of Fig. 1). Two views of RadViz3D displays of each dataset are in the middle two columns, and a 3D UMAP [12] visualization is in the right column of Fig. 1). Fig. S1 provides interactive 3D displays of RadViz3D, UMAP, t -SNE, Viz3D, and star coordinate plots with OLDA and ULDA. (OLDA, ULDA and MRP assume a low-dimensional linear subspace and require continuous variables while the default Euclidean distance used by UMAP and t -SNE is not always appropriate for mixed-features data. These methods are all also scale-variant. We use the GDT in mixed-features

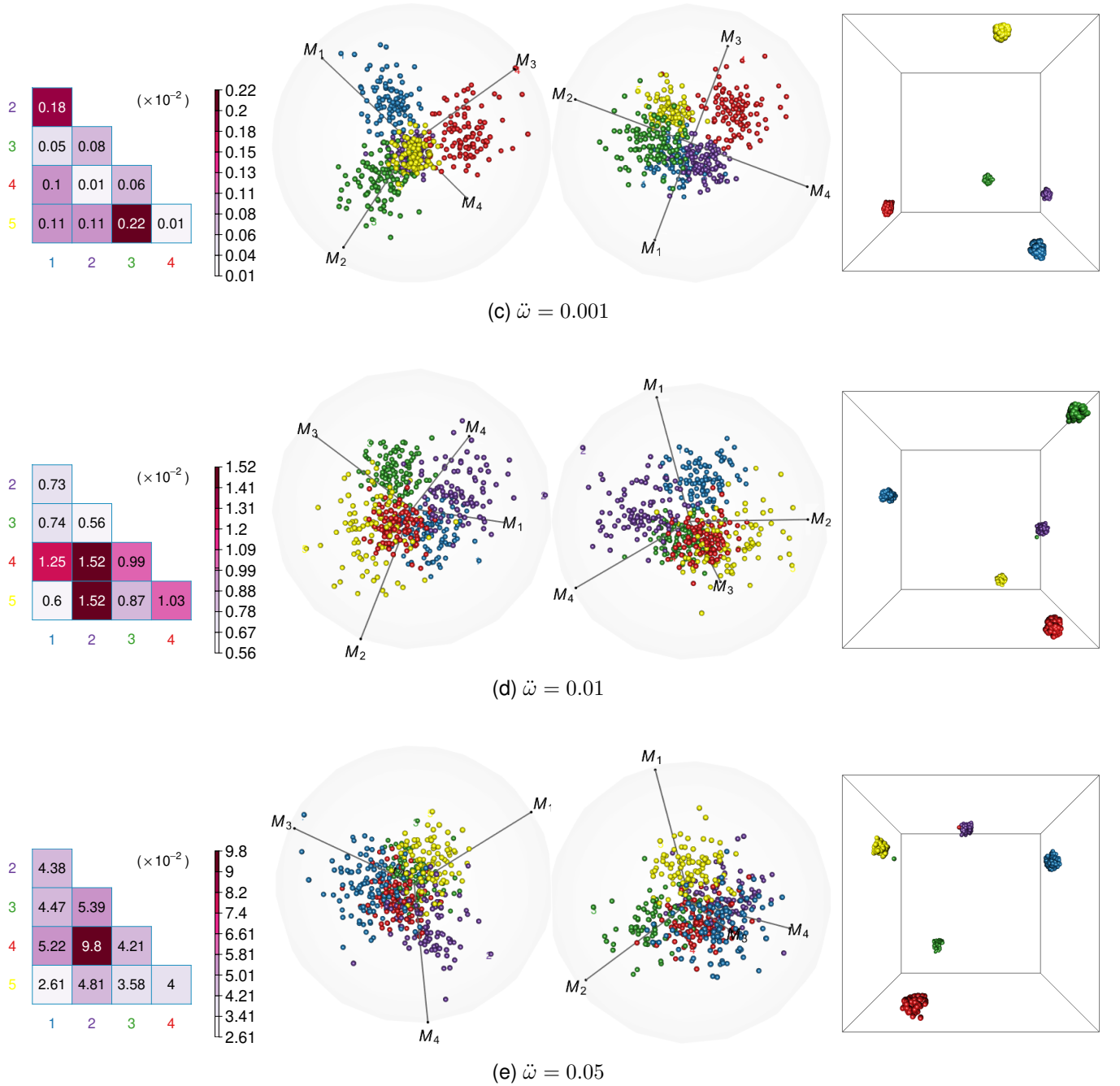


Fig. 1: Overlap maps (Ω , left) RadViz3D (middle figures) and UMAP displays (right) of simulated 100D mixed-feature datasets of varying group separation ($\tilde{\omega}$). Label colors in Ω match those in the RadViz3D displays.

datasets – itself a major contribution of the paper – to address all these issues in all methods.) Further, in discussing the different displays, we note that the objective behind accurate visualization of labeled data is the display of labels according to the actual separation between them.

Fig. 1 and Fig. S1 show that Radviz3D provides meaningful displays that track the difficulty of separation very well as $\tilde{\omega}$ increases from 0.001 through 0.01 to 0.05 (see Fig. S1 for dynamic displays for $\tilde{\omega} \in \{0.0001, 0.001, 0.01, 0.05, 0.25\}$). Further, Fig. 1a shows the highest overlap between Groups 3 and 5 and between Groups 1 and 2 is fairly accurately reproduced in the RadViz3D display. Similar patterns are also noticed in Figs. 1b

and 1c. For instance, in Fig. 1b, there are high overlaps between Groups 2 and 4 and between Groups 2 and 5, and these high overlaps, relative to the other pairs, is also reflected in the RadViz3D display. From Fig. 1c, we see that Groups 2 and 4 have the highest overlap and again RadViz3D produces a display consistent with this observation. Our illustrative experiment therefore shows RadViz3D's ability to faithfully display high-dimensional grouped datasets with varying separation. Our displays of the competing methods show that, but for UMAP, they are unable to display the separation of classes even in the case when they are generated with low $\tilde{\omega}$. UMAP (for instance, Fig. 1 can separate out classes in all cases very well, but

can not distinguish the cases when class labels are well-separated from the cases when they are not. Specifically, UMAP provides similar representation of the distinctiveness of the groups across all cases regardless of whether the groups are well- or poorly-separated (as quantified by the overlap measures). We contend that this good separation of data by labels regardless of their overlap or difficulty of separation is a desirable property of a classification algorithm but not for visualization which should faithfully render the correct status and should display well-separated labeled data as such and poorer-separated labeled data as such. In that goal, only RadViz3D provides meaningful displays.

4 REAL-DATA EXAMPLES

We now explore the visualization of datasets with continuous, discrete or mixed features. The focus of our work is on displaying high-dimensional datasets, so we provide only one moderate (9D) example. Our other examples have larger p , in some cases of several thousands. For brevity, we only have static displays here with RadViz3D, and refer to the online resource for dynamic or competing displays.

4.1 Datasets with continuous features

4.1.1 A moderate-dimensional dataset

Gamma Ray Bursts (GRBs) are the brightest electromagnetic events known to occur in space and are believed to contain

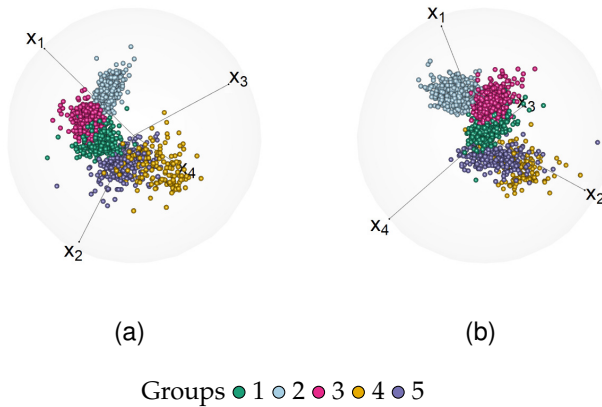


Fig. 2: RadViz3D displays of GRB dataset.

clues to the origin of the cosmos. Although the astrophysics community has long been divided on whether there are two [35] or three [36], [37] kinds of GRBs, a careful recent revisit [38], [39], [40], [41] of the clustering problem revealed that all nine available features are necessary for clustering and show overwhelming evidence of five classes of GRBs. These nine features are the two duration variables that represent the time by which 50% and 90% of the flux arrive, four time-integrated fluences in the 20-50, 50-100, 100-300 and >300 keV spectral channels and three peak fluxes in time bins of 64, 256 and 1024 milliseconds. There are very strong correlations between some of these features, leading to their summary and erroneous [39] deletion before clustering.

The BATSE 4Br catalog has complete records on 1599 GRBs. With 9 features, it can conceptually be displayed using RadViz3D or Viz3D, however we use MRP to project

the data onto a lower-dimensional space because of the very strong correlations between the features. The nine features are heavily skewed so we also employ the GDT following Remark 8. Fig. 2 displays the dataset using the multivariate t -mixtures grouping [39]. The five groups are not separated with t -SNE (Fig. S2a), star coordinates plots with OLDA (Fig. S2c) or ULDA (Fig. S2d), but more distinguishable with Viz3D (Fig. S2e) and with RadViz3D (Fig. S2f). Our display confirms the finding of five distinct classes [39]. At the same time, it also explains the earlier controversy, because it shows two or three possible super-types ($\{1, 2, 3\}$ and $\{4, 5\}$) potentially encompassing the five kinds [39] of GRB, which is better reflected by RadViz3D (Fig. S2f). Such interpretations are not possible with UMAP (Fig. S2b) which separates the five groups very distinctly.

4.1.2 High-dimensional continuous datasets

We also have illustrations on some very high-dimensional datasets, some of which also have $n \ll p$ observations.

4.1.2.1 Zipcode digits: This dataset [42], a sample of which is in Fig. 3a, is of 2000 16×16 images of handwritten Hindu-Arabic numerals and has been used to evaluate classification and clustering algorithms [41], [43]. The

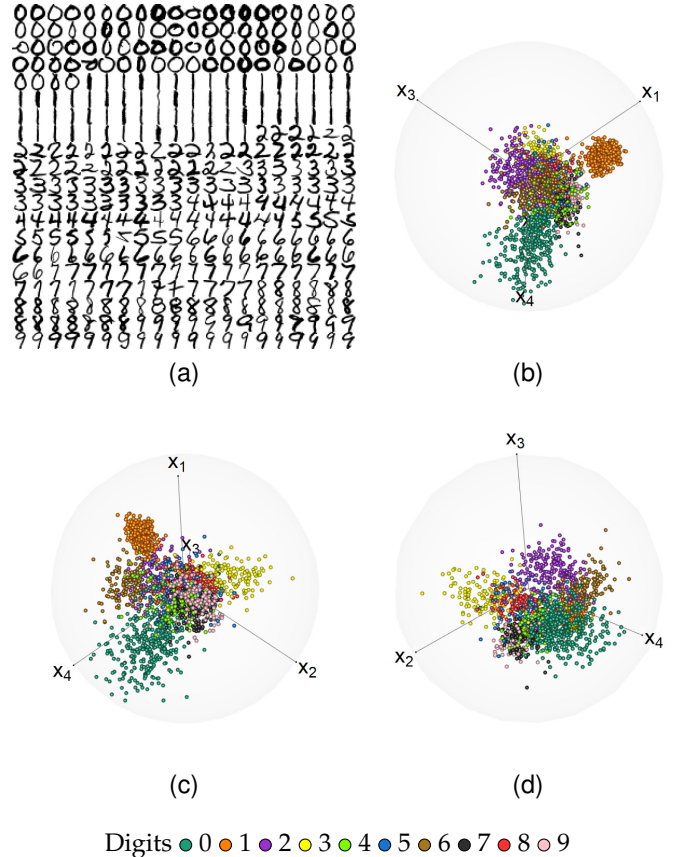


Fig. 3: (a) Random sample of the zipcode digits dataset and (b-d) three RadViz3D views of the zipcode dataset.

distributions for each group are unclear, so we use the GDT and then obtain the first four MRPs and display the dataset. Fig. S3 shows that star coordinates plots using OLDA and ULDA (with four projections) are unable to distinguish the digits while Viz3D and RadViz3D (Figs. 3b-d and S3e) on

the four MRPs) do a better job. UMAP (Fig. S3b) separates the different digits completely, but is largely unable to point out the variability in the handwriting of each digit or the complexity in the handwriting. It also breaks up “4” into two groups, merging one of them with “9.” RadViz3D and Viz3D reflect the complexity better than the others, capturing, for instance, the fact that “7” and “9” or “4” and “9” often have many similar pixel values (Fig. 3a).

4.1.2.2 Faces: The *Faces* dataset [44] has 112×92 images of 40 human faces, each at ten different light angles and conditions. We choose six individuals (Fig. 4a) and apply the wavelet transform on the Radon projection of each image [45] to address variations in facial expression, and illumination and use these reduced 280 features for our displays. The Radon projections and wavelet transforms

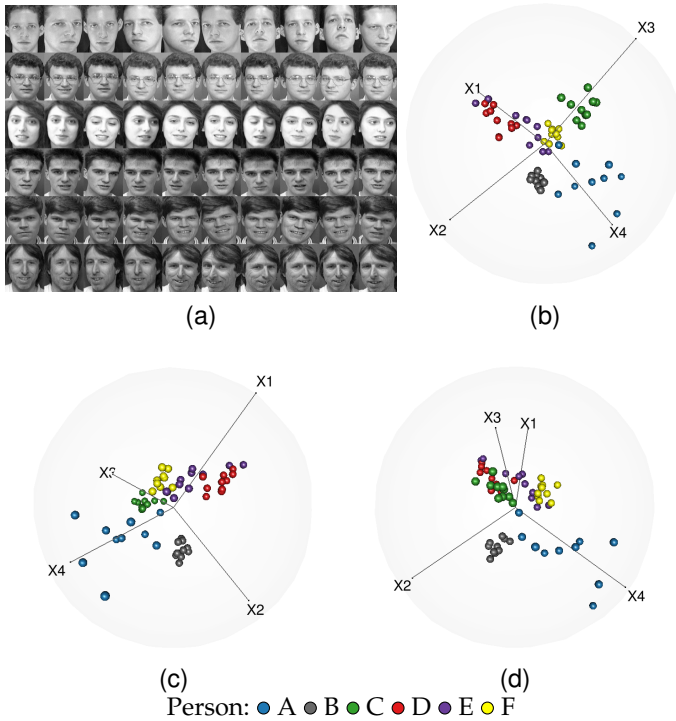


Fig. 4: (a) The set of faces and (b) its RadViz3D displays.

yield unclear marginal distributions so we use the GDT before obtaining the first 4 MRPs. The displays show poor distinction between the 6 individuals using star coordinates with OLDA (Fig. S4c) and ULDA (Fig. S4d). On the other hand, *t*-SNE (Fig. S4a), UMAP (Fig. S4b), Viz3D (Fig. S4e) and RadViz3D (Fig. S4f) are able to distinguish the 6 individuals well. But the UMAP (Fig. S4b) fails to illustrate the variability in the images from the same person, which can be reflected in the RadViz3D and Viz3D displays.

4.1.2.3 Suicide ideation: Predicting suicide is a challenging task for psychiatrists. A recent functional Magnetic Resonance Imaging study [46] gathered data based on changes in activation relative to the baseline, on 30 words, in nine suicide attempters, eight non-attempter ideators and 17 healthy controls with no personal or family history of psychiatric disorders or suicide attempts. The dataset therefore has $G=3$ groups of responses (changes in activation, relative

to the baseline) to these 30 words (which we consider as replicates, so $n = 1020$) at $p = 24660$ voxels.

Fig. 5 and Fig. S5d show that RadViz3D reasonably distinguishes these three groups, while also showing the difficulty of the problem. Viz3D (Fig. S5c) distinguishes the three groups less, and this is especially true of the control group vis-a-vis the suicide non-attempter ideators. OLDA and ULDA can not be implemented for this dataset while *t*-SNE (Fig. S5a) and UMAP (Fig. S5b) displays are very poor.

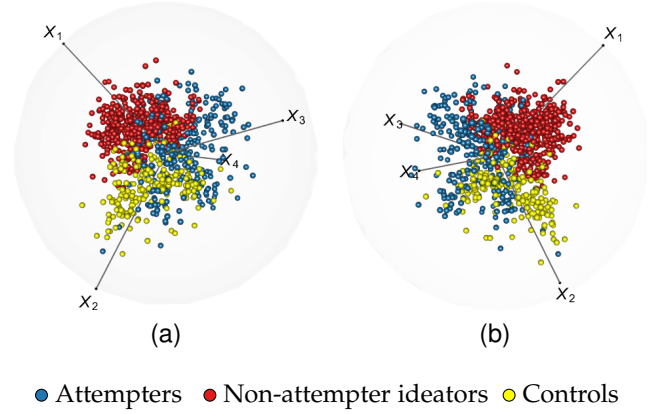


Fig. 5: Radviz3d displays of suicide ideation dataset.

4.2 Datasets with discrete features

Our next examples are on datasets with discrete features. There exist no competing methods that can handle such datasets so we use the GDT on these datasets before using them. The MRP is also used before displaying with RadViz3D, star coordinates and Viz3D displays.

4.2.1 Voting records of US senators

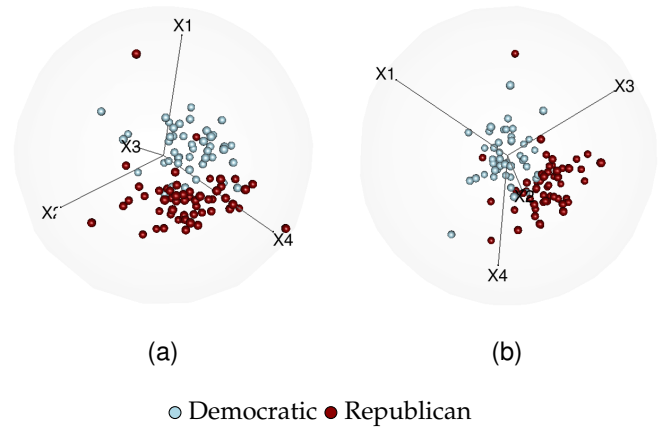


Fig. 6: RadViz3D displays of senators' voting records.

The 108th US Congress had 55 Republican and 45 Democratic (including 1 independent in the Democratic caucus) senators vote on 542 bills [47]. We display the senators according to whether they voted for each bill or not (*i.e.* against/abstained). The RadViz3D (Fig. 6, Fig. S6f) display distinguishes the 2 groups, reflecting the political affiliation. Here $G=2$, so three zero-eigenvalue projections beyond the

MRP are used in the RadViz3D display. As explained in Section 2.2.1.2, these additional projections (associated with the anchor points X_2, X_3, X_4) do not contribute towards separating the two groups which are separated solely by the first MRP (associated with X_1). A physical interpretation is that the spring on anchor point X_1 pulls one group harder than another group, separating it out, while the “null” springs on X_2, X_3, X_4 pull both groups with equal force. All anchor points are evenly-distributed on the unit sphere, so the forces applied by X_2, X_3, X_4 cancel and only the spring attached to X_1 separates the first group from the second in the visualization. RadViz3D and UMAP separate out the two groups, but RadViz3D, unlike UMAP (Fig. S6b), also gives us a sense of the closeness of some senators in either group with the other. The t -SNE (Fig. S6a), Viz3D (Fig. S6e) and especially star coordinate plots with ULDA (Fig. S6c) and OLDA (Fig. S6d) are unable to separate the two parties.

4.2.2 Adult Autism Spectrum Disorder (ASD) screening

This dataset [48] from the UCI’s Machine Learning Repository (MLR) [49] has 15 binary (and 5 additional) features on 515 normal and 189 ASD-diagnosed adults. The two groups

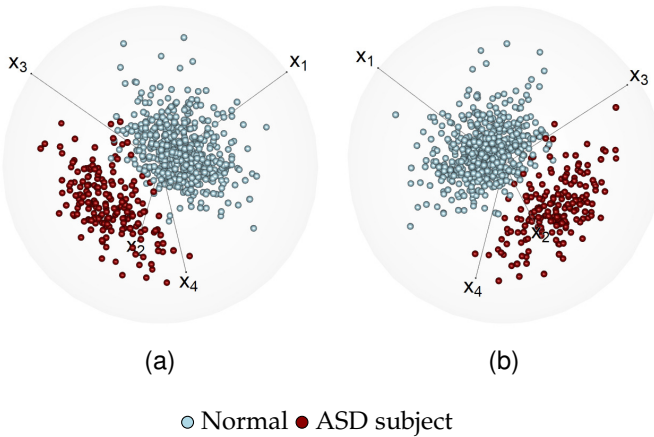


Fig. 7: RadViz3D displays of the ASD screening dataset.

are reasonably well-separated, with minimum classification error of 1.7% [50], and therefore should be easily separated. RadViz3D (Fig. 7 and Fig. S7f) performs better in separating two groups than t -SNE (Fig. S7a), star coordinates with OLDA (Fig. S7c) or ULDA (Fig. S7d), and Viz3D (Fig. S7e). UMAP (Fig. S7b) also separates the two groups, but they are completely disjoint and does not accurately reflect the best misclassification rate of 1.7% for this dataset.

4.2.3 SPECT heart dataset

This dataset [51] from the UCIMLR [49] has 22 binary attributes that summarize cardiac Single Proton Emission Computed Tomography (SPECT) images of 55 normal and 212 abnormal patients. Each image was summarized by means of 44 continuous features that was further processed to obtain 22 binary features [51]. The separation between these two groups is very good with current classification results [52] finding small but positive misclassification rates. In this example, RadViz3D (Fig. 8 and Fig. S8f) performs well in separating the two groups with very small overlap.

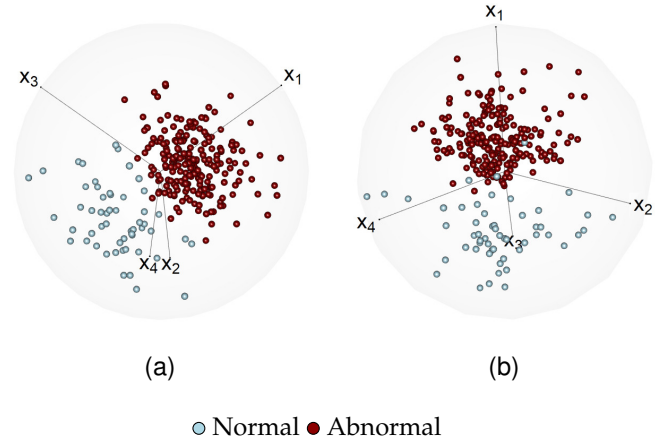


Fig. 8: RadViz3D displays of the SPECT Heart dataset.

UMAP (Fig. S7b) again produces disjoint groups in the visualization and fails to accurately reflect the non-zero misclassification rate between the two groups while t -SNE (Fig. S8a), Viz3D (Fig. S8e) and especially star coordinate plots with OLDA (Fig. S8c) or ULDA (Fig. S8d) fail to clearly display the separability of the two groups.

4.3 Datasets with mixed features

We now illustrate performance of RadViz3D on two real datasets with continuous and discrete-valued features. No method can currently display such datasets, so as in Section 4.2, we employ the GDT (and the MRP for RadViz3D and Viz3D) on the datasets before their display.

4.3.1 Indic scripts

This dataset [53] is on 116 different features from handwritten scripts of 11 Indic languages. We choose a subset of 5 languages from 4 regions, namely Bangla (from the east), Gurmukhi (north), Gujarati (west), Kannada and Malayalam (languages from the neighboring southern states of Karnataka and Kerala) and a sixth language (Urdu, with a distinct Persian script). Figure. 9a displays a line from a sample document in each script and illustrates the challenges in characterizing handwritten scripts because of the additional effect of individual handwriting styles. The challenges of accounting for handwriting variability, and the distinctiveness of the six scripts are captured well in the RadViz3D displays (Figs. 9b, 9c and S9f). For example, we see that Kannada and Malayalam are close by in the displays. The three Sanskrit-based languages of Bangla, Gujarati and Gurmukhi are neighbors of each other in the displays. The placement of Urdu farther from the rest but still close to both Gujarati and Bangla indicates the possible influence of Persian, for reasons of history and geography, on the handwriting of these scripts. The RadViz3D displays therefore make intuitive sense for this dataset. The t -SNE (Fig. S9a) and UMAP (Fig. S9b) displays distinguish the scripts very well but do not depict similarities between them. Indeed, the UMAP display separates even individuals from within the scripts, and in our view, performs poorly. Viz3D (Fig. S9e) distinguishes Urdu, Kannada and Gujarati very well but not the other languages while star coordinate plots (Figs. S9c,d) with OLDA and ULDA do poorly.

ਆਭਿ ਰੁਪਿਯਾ ਧਰਮ ਰੁਪਿਯਾ ਭ੍ਰਿਗੁ ਰੇਨਾ ਧਰਮ ਤਰਮੁ,
 ਮਾ ਕਾਏ ਲਾਤੀ ਭੇਡਾਏ ਘਾਈ ਪੀ ਲਭੀ ਜੀ ਖੀਨੀ ਪੀਲੀ ਮਈ ਪਤਾ ਲੜਕਿਆ-
 ਸਭਰਾ ਦਾ ਰਾਗੇ ਆਇਆ ਜਾ ਸਰਾ ਹੋ। ਧਰਮ ਜੋ
 ਦੁਰਗੇਸ਼ੁ ਮੋਢਿਓ ਕੋਲਨੇਦਲੀ ਲਭੇ ਦੁਰਦੁਰੀਤ ਚਨੁ
 ਆਭੀ ਰੇਨਾਮਾਭੀਰਾਮੁ, ਆਰਾਧਨਾਭੀਰਾਮੁ ਧਰਮੁ ਰਾਭੀਰਾਮੁ
 ਪੰਡਿਤਪੁਰੀਸ਼੍ਵਰੀ ਧਰਮੁ ਪੁਰੀਸ਼੍ਵਰੀ ਧਰਮੁ - ਪੰਡਿਤਪੁਰੀਸ਼੍ਵਰੀ

(a) Handwriting samples from (top to bottom) Bangla, Gujarati, Gurmukhi, Kannada, Malayalam and Urdu

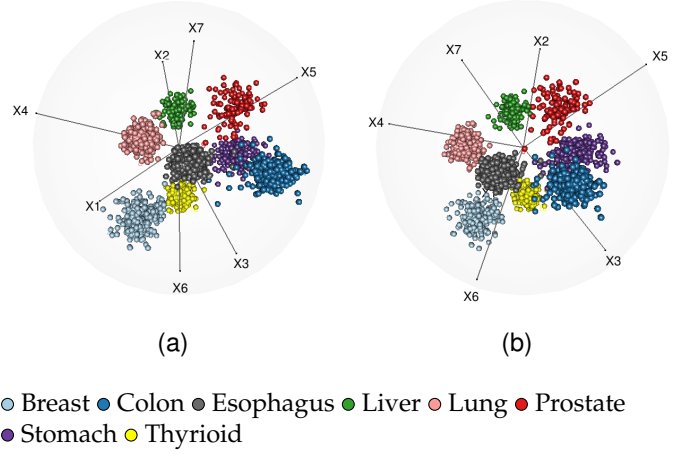


Fig. 10: RadViz3D displays of the RNA-seq dataset.

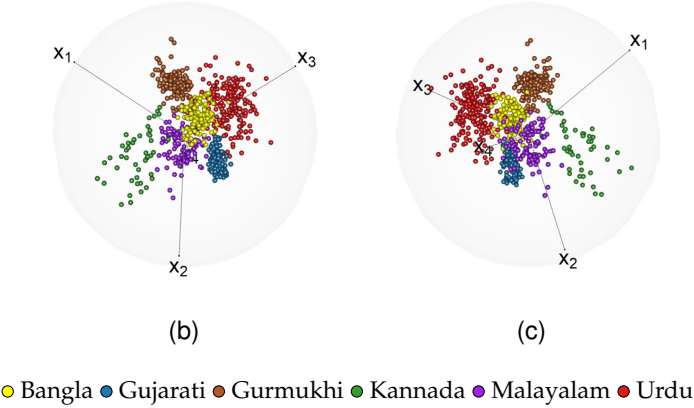


Fig. 9: Indic scripts: (a) Samples and (b,c) RadViz3D displays.

4.3.2 RNA sequences of human tissues

This dataset [54] consists of gene expression levels, in FPKM (Fragments per Kilobase of transcripts per Million), of RNA sequences from 13 human organs. from which we choose the eight largest (in terms of available samples) organs, – esophagus (659 samples), colon (339), thyroid (318), lung (313), breast (212), stomach (159), liver (115) and prostate (106) – for our illustration. This dataset has $p=20242$ discrete features, however some of them have so many discrete values, and the probabilities for these discrete values are almost equal and very small. So, these features have approximately continuous CDFs and can be considered to be continuous. Thus, this dataset essentially has both discrete and continuous attributes. The RadViz3D(Figs. 10 and S10f) display shows very clear separation between almost all the organs, except for the colon and the stomach that have marginal overlap while t -SNE (Fig. S10a) and UMAP (Fig. S10b) show unclear distinction of the organs and are unsatisfactory. Viz3D (Fig. S10e) and star coordinate plots (Figs. S10c,d) with OLDA and ULDA also perform worse than RadViz3D.

5 DISCUSSION

We develop a 3D radial visualization tool called RadViz3D that serves as an engine for displaying labeled data with mixed attributes. The placement of anchor points is shown

to be ideally as far away relative to each other as possible to avoid artificial visual correlations. This desired property motivates the use of a 3D display as it provides for larger distances between anchor points. Therefore, we provided the exact and approximate solutions for the placement of p anchor points on the sphere. Another focus of this paper is in the display of labeled high-dimensional observations. We develop the MRP to summarize a dataset before display, such that the projected data have uncorrelated coordinates while also separating the different groups. A third contribution of this paper is to display data with mixed features so we propose using the GDT to transform features to have standard normal marginals, while preserving the correlation structure using copulas. Labeled datasets with discrete-valued, mixed or heavily-skewed attributes are transformed, after removing redundant features, to the continuous space using the GDT, following which they are displayed using the MRP and RadViz3D. Our methodology displays both the distinctiveness and complexity of labeled data well. An R package `radviz3d` implementing our methodology is publicly available at <https://github.com/fanne-stat/radviz3d/>. The GDT and the MRP are general transformation and data reduction methods that we show can also be used with other visualization techniques.

Some aspects of our development could benefit from further attention. For instance, the MRP is a linear projection method that is designed to maximize separation between labeled data. It would be interesting to see if non-linear projections can improve results. Also, for unlabeled data, we suggest the use of PCs in place of the MRP, but other transformations may provide better visualizations. Also, the GDT is inapplicable to datasets with features that have more than two nominal categories. It would be important to develop methodology for such datasets. Our development of RadViz3D demonstrates that we should use (at least approximately) equi-spaced anchor points, so while investigating layouts and spacings as done [20], [55], [56] for RadViz2D is perhaps unnecessary, but the order of the anchor points is still important. The MRP provides a specific sequence for the anchor points, however, in 3D, the order is still important. The order of anchor points corresponds to switching the order of the columns in the projection

matrix U in (1). Clearly different orders of anchor points will produce different visualizations. For the visualization of labeled data, one possible solution to this is to run through all possible orders and pick one that has the biggest separation between groups, where \tilde{w} can be used to measure separation. However, this would be very computationally demanding for high-dimensional datasets. Also, based on our assumption that all coordinates are uncorrelated, the order is intuitively perhaps not as important since all the coordinates are somewhat equivalent in our display. But it would still be worth getting a definitive answer. Thus, we see that while this paper has made important contributions in visualizing mixed-attribute datasets, there remain issues that merit additional investigation.

ACKNOWLEDGMENTS

The authors thank the three reviewers and the Associate Editor for their insightful comments on an earlier version of the manuscript. We also thank S. Dutta, N. Kunwar, H. Nguyen, P. Lu, F.S. Aguilar, G. Agadilov and I. Agbemafle for helpful discussions. A version of this manuscript won the first author a 2021 Student Paper Competition award from the American Statistical Association (ASA) Section on Statistical Graphics. The third author's research was supported in part by the National Institute of Biomedical Imaging and Bioengineering (NIBIB) of the National Institutes of Health (NIH) under its Award No. R21EB016212, and by the United States Department of Agriculture (USDA)/National Institute of Food and Agriculture (NIFA), Hatch project IOW03617. The content of this paper however is solely the responsibility of the authors and does not represent the official views of either the NIBIB, the NIH or the USDA.

REFERENCES

- [1] S. K. Card, J. D. Mackinlay, and B. Schneiderman, *Readings in information visualization: using vision to think*. Morgan Kaufmann, 1999.
- [2] E. Bertini, A. Tatu, and D. Keim, "Quality metrics in high-dimensional data visualization: an overview and systematization," *IEEE Transactions on Visualization and Computer Graphics*, vol. 17, no. 12, p. 2203–2212, 2011.
- [3] J. M. Chambers, W. S. Cleveland, B. Kleiner, and P. A. Tukey, *Graphical Methods for Data Analysis*. Belmont, CA: Wadsworth, 1983.
- [4] H. Chernoff, "The use of faces to represent points in k-dimensional space graphically," *Journal of the American Statistical Association*, vol. 68, no. 342, pp. 361–368, 1973.
- [5] A. Inselberg, "The plane with parallel coordinates," *The Visual Computer*, vol. 1, pp. 69–91, 1985.
- [6] E. Wegman, "Hyperdimensional data analysis using parallel coordinates," *Journal of the American Statistical Association*, vol. 85, pp. 664–675, 1990.
- [7] U. Fayyad, G. Grinstein, and A. Wierse, *Information Visualization in Data Mining and Knowledge Discovery*. Morgan Kaufmann, 2001.
- [8] D. F. Andrews, "Plots of high-dimensional data," *Biometrics*, vol. 28, no. 1, pp. 125–136, 1972.
- [9] R. Khattree and D. N. Naik, "Andrews plots for multivariate data: Some new suggestions and applications," *Journal of Statistical Planning and Inference*, vol. 100, no. 2, pp. 411–425, 2002.
- [10] K. R. Gabriel, "The biplot graphical display of matrices with application to principal component analysis," *Biometrika*, vol. 58, pp. 453–467, 1971.
- [11] E. Kandogan, "Visualizing multi-dimensional clusters, trends, and outliers using star coordinates," in *Proceedings of the Seventh ACM SIGKDD International Conference on Knowledge Discovery and Data Mining*, ser. KDD '01. New York, NY, USA: ACM, 2001, pp. 107–116. [Online]. Available: <https://doi.acm.org/10.1145/502512.502530>
- [12] L. McInnes, J. Healy, N. Saul, and L. Grossberger, "Umap: Uniform manifold approximation and projection," *Journal of Open Source Software*, vol. 3, p. 861, 09 2018.
- [13] P. Hoffman, G. Grinstein, K. Marx, I. Grosse, and E. Stanley, "DNA visual and analytic data mining," in *Proceedings of the 8th conference on Visualization '97, VIS'97*. IEEE Computer Society Press, 1997, p. 437–441.
- [14] P. Hoffman, G. Grinstein, and D. Pinkney, "Dimensional anchors: a graphic primitive for multidimensional multivariate information visualizations," in *Proceedings of the 1999 workshop on new paradigms in information visualization and manipulation in conjunction with the eighth ACM international conference on Information and knowledge management*. ACM, 1999, pp. 9–16.
- [15] G. G. Grinstein, C. B. Jessee, P. E. Hoffman, P. J. O'Neil, and A. G. Gee, "High-dimensional visualization support for data mining gene expression data," in *DNA Arrays: Technologies and Experimental Strategies*, E. V. Grigorenko, Ed. Boca Raton, Florida: CRC Press LLC, 2001, ch. 6, pp. 86–131.
- [16] G. M. Draper, Y. Livnat, and R. F. Riesenfeld, "A survey of radial methods for information visualization," *IEEE Transactions on Visualization and Computer Graphics*, vol. 15, no. 5, pp. 759–776, Sep. 2009.
- [17] A. O. Artero and M. C. F. de Oliveira, "Viz3d: effective exploratory visualization of large multidimensional data sets," in *Proceedings. 17th Brazilian Symposium on Computer Graphics and Image Processing*, Oct 2004, pp. 340–347.
- [18] K. Daniels, G. Grinstein, A. Russell, and M. Glidden, "Properties of normalized radial visualizations," *Information Visualization*, vol. 11, no. 4, pp. 273–300, 2012. [Online]. Available: <https://doi.org/10.1177/1473871612439357>
- [19] M. Ankerst, D. Keim, and H. P. Kriegel, "Circle segments: a technique for visually exploring large multidimensional data sets," *Human Factors*, vol. 1501, pp. 5–8, 1996.
- [20] L. di Caro, V. Frias-Martinez, and E. Frias-Martinez, "Analyzing the role of dimension arrangement for data visualization in Radviz," in *Advances in Knowledge Discovery and Data Mining*. Springer, 2010, p. 125–132.
- [21] J. Sharko, G. Grinstein, and K. A. Marx, "Vectorized Radviz and its application to multiple cluster datasets," *IEEE Transactions on Visualization and Computer Graphics*, vol. 14, no. 6, pp. 1444–1451, December 2008.
- [22] A. González, "Measurement of areas on a sphere using Fibonacci and latitude-longitude lattices," *Mathematical Geosciences*, vol. 42, p. 49, january 2010.
- [23] M. Atiyah and P. Sutcliffe, "Polyhedra in physics, chemistry and geometry," *Milan Journal of Mathematics*, vol. 71, no. 1, pp. 33–58, Sep 2003. [Online]. Available: <https://doi.org/10.1007/s00032-003-0014-1>
- [24] E. B. Saff and A. B. Kuijlaars, "Distributing many points on a sphere," *The mathematical intelligencer*, vol. 19, dec 1997.
- [25] Y. Koren and L. Carmel, "Robust linear dimensionality reduction," *IEEE Transactions on Visualization and Computer Graphics*, vol. 10, no. 4, pp. 459–470, July 2004.
- [26] G. Golub, C. Van Loan, C. Van Loan, and P. Van Loan, *Matrix Computations*, ser. Johns Hopkins Studies in the Mathematical Sciences. Johns Hopkins University Press, 1996. [Online]. Available: <https://books.google.com/books?id=mlOa7wPX6OYC>
- [27] J. Ye, "Characterization of a family of algorithms for generalized discriminant analysis on undersampled problems," *Journal of Machine Learning Research*, vol. 6, no. 4, 2005.
- [28] Z. Jin, J.-Y. Yang, Z.-S. Hu, and Z. Lou, "Face recognition based on the uncorrelated discriminant transformation," *Pattern recognition*, vol. 34, no. 7, pp. 1405–1416, 2001.
- [29] L. Rüschendorf, *Mathematical Risk Analysis*. Berlin Heidelberg: Springer-Verlag, 2013.
- [30] Y. Benjamini and Y. Hochberg, "Controlling the false discovery rate: a practical and powerful approach to multiple testing," *Journal of the Royal Statistical Society*, vol. 57, pp. 289–300, 1995.
- [31] V. Melnykov, W.-C. Chen, and R. Maitra, "MixSim: An R package for simulating data to study performance of clustering algorithms," *Journal of Statistical Software*, vol. 51, no. 12, pp. 1–25, 2012. [Online]. Available: <http://www.jstatsoft.org/v51/i12/>
- [32] R Development Core Team, *R: A Language and Environment for Statistical Computing*, R Foundation for Statistical Computing, Vienna, Austria, 2018, ISBN 3-900051-07-0. [Online]. Available: <http://www.R-project.org>

- [33] R. Maitra and V. Melnykov, "Simulating data to study performance of finite mixture modeling and clustering algorithms," *Journal of Computational and Graphical Statistics*, vol. 19, no. 2, pp. 354–376, 2010.
- [34] V. Melnykov and R. Maitra, "CARP: Software for fishing out good clustering algorithms," *Journal of Machine Learning Research*, vol. 12, pp. 69–73, 2011.
- [35] C. Kouveliotou, C. A. Meegan, G. J. Fishman, N. P. Bhat, M. S. Briggs, T. M. Koshut, W. S. Paciesas, and G. N. Pendleton, "Identification of two classes of gamma-ray bursts," *Astrophysical Journal Letters*, vol. 413, pp. L101–L104, Aug. 1993.
- [36] S. Mukherjee, E. D. Feigelson, G. Jogesh Babu, F. Murtagh, C. Frayley, and A. Raftery, "Three Types of Gamma-Ray Bursts," *Astrophysical Journal*, vol. 508, pp. 314–327, Nov. 1998.
- [37] I. Horváth, "A further study of the batse gamma-ray burst duration distribution," *Astronomy and Astrophysics*, vol. 392, no. 3, pp. 791–793, 2002. [Online]. Available: <http://dx.doi.org/10.1051/0004-6361/20020808>
- [38] S. Chattopadhyay and R. Maitra, "Gaussian-mixture-model-based cluster analysis finds five kinds of gamma-ray bursts in the batse catalogue," *Monthly Notices of the Royal Astronomical Society*, vol. 469, no. 3, pp. 3374–3389, 2017. [Online]. Available: <http://dx.doi.org/10.1093/mnras/stx1024>
- [39] —, "Multivariate t-mixtures-model-based cluster analysis of batse catalog establishes importance of all observed parameters, confirms five distinct ellipsoidal sub-populations of gamma ray bursts," *Monthly Notices of the Royal Astronomical Society*, vol. 481, no. 3, pp. 3196–3209, Dec. 2018.
- [40] N. Berry and R. Maitra, "TiK-means: Transformation-infused k -means clustering for skewed groups," *Statistical Analysis and Data Mining – The ASA Data Science Journal*, vol. 12, no. 3, pp. 223–233, 2019.
- [41] I. A. Almodóvar-Rivera and R. Maitra, "Kernel-estimated non-parametric overlap-based syncytial clustering," *Journal of Machine Learning Research*, vol. 21, no. 122, pp. 1–54, 2020.
- [42] W. Stuetzle and R. Nugent, "A generalized single linkage method for estimating the cluster tree of a density," *Journal of Computational and Graphical Statistics*, 2010.
- [43] A. D. Peterson, A. P. Ghosh, and R. Maitra, "Merging k -means with hierarchical clustering for identifying general-shaped groups," *Stat*, vol. 7, no. 1, p. e172, 2018.
- [44] F. S. Samaria and A. C. Harter, "Parameterisation of a stochastic model for human face identification," in *Proceedings of 1994 IEEE Workshop on Applications of Computer Vision*, Dec 1994, pp. 138–142.
- [45] D. V. Jadhav and R. S. Holambe, "Feature extraction using radon and wavelet transforms with application to face recognition," *Neurocomputing*, vol. 72, no. 7, pp. 1951–1959, 2009, advances in Machine Learning and Computational Intelligence. [Online]. Available: <http://www.sciencedirect.com/science/article/pii/S0925231208003135>
- [46] M. Adam Just, L. Pan, V. L. Cherkassky, D. L. McMakin, C. Cha, M. Nock, and D. Brent, "Machine learning of neural representations of suicide and emotion concepts identifies suicidal youth," *Nature Human Behaviour*, vol. 1, pp. 911–919, 12 2017.
- [47] O. Banerjee, L. E. Ghaoui, and A. d'Aspremont, "Model selection through sparse maximum likelihood estimation for multivariate gaussian or binary data," *Journal of Machine Learning Research*, vol. 9, pp. 485–516, 2008.
- [48] F. Thabtah, "Autism spectrum disorder screening: machine learning adaptation and DSM-5 fulfillment," in *Proceedings of the 1st International Conference on Medical and Health Informatics 2017*. ACM, 2017, pp. 1–6.
- [49] D. J. Newman, S. Hettich, C. L. Blake, and C. J. Merz, "UCI repository of machine learning databases," 1998. [Online]. Available: [http://www.ics.uci.edu/\\$sim\\$mllearn/MLRepository.html](http://www.ics.uci.edu/simmllearn/MLRepository.html)
- [50] S. Raj and S. Masood, "Analysis and detection of autism spectrum disorder using machine learning techniques," *Procedia Computer Science*, vol. 167, pp. 994–1004, 2020, international Conference on Computational Intelligence and Data Science.
- [51] L. A. Kurgan, K. J. Cios, R. Tadeusiewicz, M. R. Ogiela, and L. S. Goodenday, "Knowledge discovery approach to automated cardiac SPECT diagnosis," *Artificial Intelligence in Medicine*, vol. 23, no. 2, pp. 149–169, 2001.
- [52] S. S. Yadav, S. M. Jadhav, R. G. Bonde, and S. T. Chaudhari, "Automated cardiac disease diagnosis using support vector machine," in *2020 3rd International Conference on Communication System, Computing and IT Applications (CSCITA)*, 2020, pp. 56–61.
- [53] S. M. Obaidullah, C. Halder, K. C. Santosh, N. Das, and K. Roy, "Phdindic_11: page-level handwritten document image dataset of 11 official indic scripts for script identification," *Multimedia Tools and Applications*, vol. 77, no. 2, pp. 1643–1678, Jan 2018. [Online]. Available: <https://doi.org/10.1007/s11042-017-4373-y>
- [54] Q. Wang, J. Armenia, C. Zhang, A. Penson, E. Reznik, L. Zhang, T. Minet, A. Ochoa, B. Gross, C. A. Iacobuzio-Donahue, D. Betel, B. S. Taylor, J. Gao, and N. Schultz, "Unifying cancer and normal RNA sequencing data from different sources," *Scientific Data*, vol. 5, p. 180061, 04 2018.
- [55] T. van Long and V. T. Ngan, "An optimal radial layout for high dimensional data class visualization," in *2015 International Conference on Advanced Technologies for Communications (ATC)*, 2015, pp. 343–346.
- [56] S. Cheng, W. Xu, and K. Mueller, "Radviz Deluxe: An attribute-aware display for multivariate data," *Processes*, vol. 5, p. 75, 2017.

Yifan Zhu received the Bachelor of Mathematics degree from Xi'an Jiaotong University, School of Mathematics and Statistics in 2016 and the Master of Science (MS) degree in Statistics from Iowa State University in 2019. He is currently a fifth-year PhD student in the Department of Statistics at Iowa State University under Professor Ranjan Maitra. His research interests include dimensionality reduction and classification for high dimensional discrete datasets, copula models and clustering algorithms. His work on this paper won the 2021 ASA Section on Statistical Graphics student paper award.

Fan Dai received the Bachelor of Statistics degree from Shanghai University of Finance and Economics, School of Statistics and Management in 2013, the MS degree in Statistical and Economic Modeling from Duke University in 2015 and the PhD degree in Statistics from Iowa State University in 2020. She is currently a tenure track Assistant Professor of Statistics in the Department of Mathematical Sciences at Michigan Technological University. Her research interests include statistical inference on high-dimensional directional data, geometrically anisotropic spatial process and spatial model estimation with matrix-free computation methods and Bayesian approach. She won the 2020 ASA Section on Statistical Computing student paper award.

Ranjan Maitra received the Bachelor of Statistics (with Honours) and Master of Statistics degrees from the Indian Statistical Institute (ISI), Calcutta, India in 1990 and 1992, respectively, and the PhD degree in statistics from the University of Washington in 1996. He is Professor in the Department of Statistics at Iowa State University, whose faculty he joined as tenured Associate Professor in 2003. His prior appointments were as Research Scientist in the Statistical Analysis and Data Mining Research group at Bell Communications Research, and as tenure-track Assistant Professor and tenured Associate Professor in the Department of Mathematics and Statistics at the University of Maryland, Baltimore County. His research interests include the analysis of massive datasets, computational statistics, cluster analysis, data mining, efficient simulation algorithms, image analysis and statistical computing. He received best paper and poster awards in 1995, 1996, 1996 and 1998 and the National Science Foundation's (NSF) CAREER award in 2003. He was elected Fellow of the American Statistical Association (ASA) and also elected Member of the International Statistical Institute, both in 2011. He has been Editor of the multi-society-sponsored journal *Statistics Surveys* since 2010 and was the 2018–20 Area Editor (Applications) for the ASA-sponsored journal *Statistical Analysis and Data Mining – The ASA Data Science Journal*. He is a standing committee member of the National Institutes of Health study section on the Neural Basis of Psychopathology, Addictions and Sleep Disorders since 2018. His research has been funded by the NSF, the National Institutes of Health, the National Institute of Justice and the National Oceanographic and Atmospheric Administration. Seven of his mentored students won ASA student paper competition awards in 2011, 2012, 2014, 2018, 2020 and 2021.